SA2RAGE: A New Sequence for Fast B_1^+-Mapping

Florent Eggenschwiler,[1] Tobias Kober,[1,2] Arthur W. Magill,[1,3] Rolf Gruetter,[1,3,4] and José P. Marques[1,3]*

At high magnetic field strengths ($\geq$3T), the radiofrequency wavelength used in MRI is of the same order of magnitude of (or smaller than) the typical sample size, making transmit magnetic field (B_1^+) inhomogeneities more prominent. Methods such as radiofrequency-shimming and transmit SENSE have been proposed to mitigate these undesirable effects. A prerequisite for such approaches is an accurate and rapid characterization of the B_1^+ field in the organ of interest. In this work, a new phase-sensitive three-dimensional B_1^+-mapping technique is introduced that allows the acquisition of a 64 × 64 × 8 B_1^+-map in ~20 s, yielding an accurate mapping of the relative B_1^+ with a 10-fold dynamic range (0.2–2 times the nominal B_1^+). Moreover, the predominant use of low flip angle excitations in the presented sequence minimizes specific absorption rate, which is an important asset for in vivo B_1^+-shimming procedures at high magnetic fields. The proposed methodology was validated in phantom experiments and demonstrated good results in phantom and human B_1^+-shimming using an 8-channel transmit-receive array. Magn Reson Med 67:1609–1619, 2012. © 2011 Wiley Periodicals, Inc.

Key words: SA2RAGE; B_1^+-mapping; B_1^+-shimming

INTRODUCTION

At high magnetic field strengths ($\geq$3T), the radiofrequency (RF) wavelength used in MRI becomes smaller than the typical sample size, making transmit magnetic field (B_1^+) inhomogeneities more prominent. RF-shimming (1) and transmit SENSE (2,3) or combinations of these methods (4) have been proposed to mitigate these B_1^+ variations. However, a prerequisite of such methods is to accurately map the B_1^+ field in short experimental times.

Several approaches had been developed in the past 20 years to determine the B_1^+ distribution. The technique of most straightforward implementation is the double-angle method (DAM), which calculates B_1^+ from the ratio of two images acquired by using flip angles α_1 and $\alpha_2 = 2\alpha_1$ and a very long repetition time (5). Another approach relies on a sequence made of three RF pulses (α, 2α, α) in order to generate both a spin echo and stimulated echo signal, which encode the transmit magnetic field information (6,7). Recently, a technique dubbed actual flip angle imaging has been introduced where two images are acquired after excitations with the same flip angle α but different repetition times TR_1 and TR_2 (8). An appropriate choice of TR_1 and TR_2 removes the T_1-sensitivity of ratio between the two signals, which therefore only depends on B_1^+ and TR_2/TR_1. Another method uses the 180° signal null to build a flip angle map (9). An innovative approach consists in the measurement of B_1^+ from the phase of the MR signal (10,11). Recently, with the availability of higher magnetic fields (implying increased B_1^+ inhomogeneity) and multiple transmit channels, B_1^+ measurements have become increasingly important, and many new methodologies have been proposed (12–18).

One of the main challenges for any B_1^+-mapping strategy to be used in the context of high static magnetic fields and parallel transmission is the range in which the measured B_1^+ is accurate and precise. A B_1^+ mapping methodology should have a large range where the assumptions made to calculate B_1^+ are valid, and the B_1^+ calculation should in that range be well conditioned (i.e the measured B_1^+ field should not be too sensitive to noise on the original images). To illustrate the importance of the large range of accuracy needed for B_1^+-mapping techniques, at 7T, the conventional circularly polarized mode (used to combine the phases of the different transmit elements) can generate B_1^+ values inside the human head that vary 4-fold, from 0.4 to 1.6 of the nominal flip angle (19,20). When using localized arrays for transmission, in which case the RF field of each coil has to be mapped, the range of B_1^+ values is even greater (with regions distal to the coil having very low B_1^+ amplitudes). The impact of the local coils on the range of accuracy required when performing the B_1^+-mapping can be somewhat reduced by using recently proposed interferometry techniques (18,21). This is achieved through the measurement of the B_1^+ field generated by a combination of coils rather than by one coil at a time. Such methods, as well as B_1^+-shimming and transmit SENSE methods, require the B_1^+-mapping technique to be sensitive to the phase of B_1^+, which is not the case when using approaches that rely on the image phase to encode the B_1^+ amplitude (10,11), or techniques where the B_1^+ of one specific channel is measured with signal acquired by all channels (17).

Often, the effect of T_1 relaxation and B_1^+ inhomogeneity on signal are intertwined, and some techniques effectively measure these two quantities simultaneously (12,13,18,22), which impacts on the signal to noise ratio

[1]Laboratory for Functional and Metabolic Imaging, Ecole Polytechnique Fédérale de Lausanne, Lausanne, Switzerland.

[2]Advanced Clinical Imaging Technology, Siemens Medical Solutions-CIBM, Lausanne, Switzerland.

[3]Department of Radiology, University of Lausanne, Lausanne, Switzerland.

[4]Department of Radiology, University of Geneva, Geneva, Switzerland.

*Correspondence to: José P. Marques, EPFL SB IPSB LIFMET, Station 6, CH-1015 Lausanne, Switzerland. E-mail: jose.marques@epfl.ch
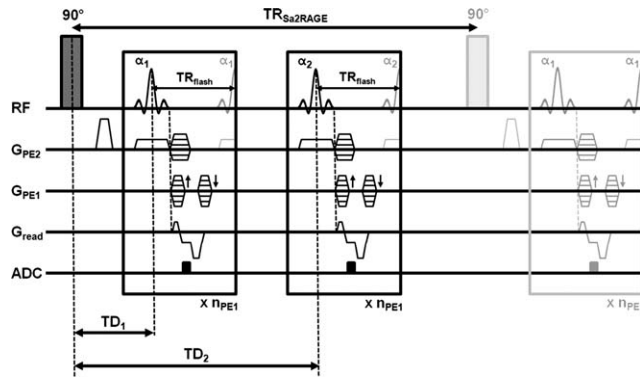
FIG. 1. SA2RAGE sequence. A 90° RF saturation pulse is followed by two gradient echo blocks. The excitation pulses of low flip angles α_1 and α_2 within the gradient recalled echo (GRE) blocks are separated by a short repetition time TR_{flash}. Each readout gradient is followed by a spoiling gradient. A strong crusher gradient is also applied in the second phase encoding direction (PE2) after the saturation pulse. During each block, all n_{PE1} phase encoding lines of the second dimension are acquired. The sequence is repeated n_{PE2} times in order to acquire all third dimension k-space planes. Each GRE block was RF spoiled so that the assumption of no transverse magnetization prior to the following excitation can be considered valid (see Appendix 2).

(SNR) efficiency of the method, or have to rely on very long repetition times to guarantee full longitudinal relaxation, at the cost of an increased measurement time. One approach proposed to overcome the need of prohibitively long repetition times in the DAM is to use saturation pulses (23). Such an approach is difficult to implement at high fields, due to the high B_1^+ inhomogeneity. Furthermore, as the static magnetic field increases, the energy associated with a similar RF pulse increases quadratically with the reference frequency and hence specific absorption rate (SAR) considerations become increasingly important, effectively limiting the power of RF pulse amplitudes and slew rate of a given sequence or implying an increase of the repetition times used. Hence, a sequence for fast B_1^+-mapping to be used at high static magnetic fields should be mostly based on low flip angle excitations. Given the large B_1^+ variations

over the body it is important to be able to perform the mapping over the entire volume either via three-dimensional (3D) sampling or interleaved multislice. Multi-slice-based methods have the disadvantage that their precision can depend on the quality of the slice selection profile, which varies as large flip angles are applied.

In this article, we propose a novel scheme, saturation-prepared with 2 rapid Gradient Echoes (SA2RAGE), which allows the 3D B_1^+-mapping of a human brain in under a minute with high precision over a large range of B_1^+ values. This method combines pulses with high and low flip angles in order to quickly measure the B_1^+ field with low SAR and is demonstrated in phantoms and in vivo studies at 7T.

METHODS

The proposed sequence SA2RAGE (Fig. 1) can either be seen as a fast saturation recovery sequence with two different delay times, or as two images acquired in a turbo flash manner separated by a saturation pulse. The images acquired just after a saturation pulse and before the following one were named $SA2RAGE_1$ and $SA2RAGE_2$, respectively. To reduce T_1-sensitivity, the first delay time (TD_1) was minimized while the second (TD_2) was maximized, making the ratio between the two acquired signals $SA2RAGE_1/SA2RAGE_2 = SA2RAGE_{ratio}$ mostly dependent on the saturation pulse performance. The predicted steady-state $SA2RAGE_{ratio}$ for several B_1^+ values was numerically calculated by solving the Bloch equations (see Appendix 1). The observed signal was considered to arise from the point where the center of k-space was acquired (19). Both the saturation pulse and the GRE acquisitions were gradient spoiled (see Fig. 1). Furthermore an RF spoiling with a 50° phase increment (24), was used within each GRE block. A lookup table between $SA2RAGE_{ratio}$ and B_1^+ values was then established from the numerical calculations (cf. Fig. 2a).

To guarantee a large range of accuracy on the B_1^+ estimation without compromising the total acquisition time simulations were performed to determine the optimum parameters of the SA2RAGE sequence.
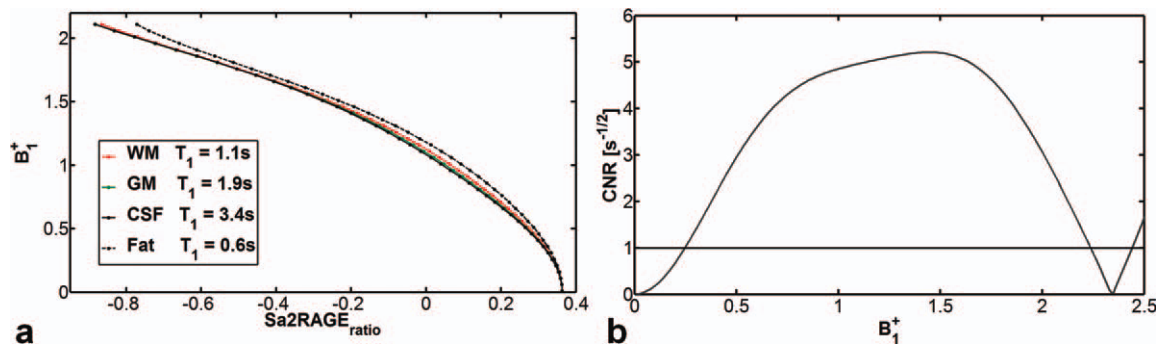

FIG. 2. **a**: Dependence of B_1^+ on $SA2RAGE_{ratio}$ for protocol A ($TR_{SA2RAGE}/TD_2$=2.4/1.8s, $\alpha_1/\alpha_2 = 4°/11°$, $n_{PE1} = 64$) and different brain tissues (cerebrospinal fluid - CSF, grey matters - GM, white matter - WM and fat whose T_1's belong to the interval 0.6–3.4 s). The B_1^+ values are presented as relative multiplicative factor of the expected B_1 field. **b**: CNR curve corresponding to the optimum parameters of the SA2RAGE sequence. The horizontal line represents $CNR_{threshold}$ and allows the visualization of the interval inside which B_1^+ can be measured above an acceptable noise level. [Color figure can be viewed in the online issue, which is available at wileyonlinelibrary.com.]

The contrast-to-noise ratio per unit of time (CNR) of the estimated $B_{1,i}^+$ in respect to a neighbouring $B_{1,i+1}^+$ amplitude was defined as:

$$\text{CNR}_{B_{1,i}^+} = \frac{(B_{1,i+1}^+ - B_{1,i}^+)}{\sqrt{\sigma_{B_{1,i+1}}^2 + \sigma_{B_{1,i}}^2}} \frac{1}{\sqrt{\text{TR}_{\text{SA2RAGE}}}} \qquad [1]$$

where $B_{1,i}^+$ and $B_{1,i+1}^+$ represent two sequential B_1^+ values. The noise of the $B_{1,i}^+$, $\sigma_{B1,i}$, was calculated via error propagation of the noise in the measurement of the SA2RAGE$_1$ and SA2RAGE$_2$ signals, into the SA2RAGE$_{\text{ratio}}$ and subsequently arising from the lookup table interpolation:

$$\sigma_{B_{1,i}^+}^2 = \left| \frac{\partial B_1^+}{\partial \text{SA2RAGE}_{\text{ratio}}} \right|_{B_1^+ = B_{1,i}^+}^2 \sigma_{\text{SA2RAGE}_{\text{ratio}}}^2$$

$$= \left| \frac{\partial B_1^+}{\partial \text{SA2RAGE}_{\text{ratio}}} \right|_{B_1^+ = B_{1,i}^+}^2 \frac{\text{SA2RAGE}_1^2 + \text{SA2RAGE}_2^2}{\text{SA2RAGE}_2^4} \sigma^2 \quad [2]$$

The first term, corresponding to the noise amplification due to the interpolation, was numerically calculated from the lookup table of SA2RAGE$_{\text{ratio}}$ as a function of the transmit field. The second term, corresponding to the noise propagation from the original images into SA2RAGE$_{\text{ratio}}$, is analytically calculated via error propagation theory. As the acquisition of each image was performed under the same conditions (acquisition bandwidth and resolution), their noise was assumed to be identical, i.e., $\sigma_{\text{SA2RAGE1}} = \sigma_{\text{SA2RAGE2}} = \sigma$. For each set of sequence parameters, CNR was computed for values of relative B_1^+ varying from 0.01 to 2.51 (in steps of 0.025), creating a CNR curve as a function of B_1^+ (see Eq. 1) that represents the ability to distinguish consecutive B_1^+ values in the presence of noise on the original images. In this work, the B_1^+ values are presented as relative multiplicative factor of the expected B_1 field. A threshold CNR value (CNR$_{\text{threshold}}$) was then experimentally derived. Subsequently, B_1^+ related to CNR values higher than this threshold were deemed as being accurately estimated. For the sake of simplicity, σ was set such that the value of CNR$_{\text{threshold}}$ corresponds to one (cf. Fig. 2b), meaning that above this threshold a change of relative B_1^+ of 0.025 can be measured.

Given the widespread range of B_1^+ values found at high fields, simulations were performed with the aim to maximize the width of CNR curve over CNR$_{\text{threshold}}$. To reduce the number of variables to evaluate, the following assumptions were made: (a) the number of excitations per GRE module (n_{PE1}) was set to 64 and TR$_{\text{Flash}}$ to 2.9 ms; (b) TD$_1$ was kept at a minimum value (given the above mentioned settings of n_{PE1} and TR$_{\text{Flash}}$) of 101 ms; (c) $T_1 = 1.5$ s was considered for all in vivo experiments (this value corresponds to the average T_1 in the brain). Concerning in vitro measurements, $T_1 = 0.8$ s was used for the experiments conducted with an oil phantom whereas an average $T_1 = 1.5$ s was considered when using an agar gel head phantom. The parameters varied were: (i) the repetition time TR$_{\text{SA2RAGE}}$ (from 1.5 to 3.5 s in steps of 0.1 s); (ii) TD$_2$ (from 1.3 to 3.4 s in steps of 0.1 s); (iii) α_1 and α_2 (varied independently from 1–10 and 1–20°, respectively).

The SA2RAGE sequence was subsequently improved in terms of T_1-insensitivity by allowing the minimal value of TD$_1$ and n_{PE1} to be further reduced. The center of k-space can be acquired earlier when either partial Fourier or parallel imaging acceleration (GRAPPA) (25) is applied in the phase encoding direction (cf. Fig. 1) leading to the possibility to choose TD$_1$ significantly smaller than 101 ms. These modifications were evaluated via numerical simulations and in vivo measurements.

In vitro and in vivo scans were performed on a Siemens 7T parallel transmit (PTx) system (Siemens Healthcare, Germany) equipped with a custom-designed 8-channel transmit-receive array coil (Rapid Biomedical, Germany). The experimental protocol was approved by local ethics committee, and one healthy subject providing informed consent was scanned. For subject safety, simulations of the RF coil were performed and the worst case scenario (sum of in phase electric fields over the whole brain) implied that the maximum power delivered by each coil element was limited to 0.9 W/10 s and 0.3 W/6 min.

The SA2RAGE$_{\text{ratio}}$ signal (computed by division of the complex images SA2RAGE$_1$ and SA2RAGE$_2$) was acquired with the sequence parameters optimized above and using a matrix size of 64 × 64 × 16 and nominal resolution of 3 × 3 × 5 mm^3. The GRE excitation pulses were slab-selective, while the saturation was a hard pulse. The specific sequence parameters used will be given throughout the results section. B_1^+ values were computed using a lookup table created as described in the Appendix 1 using the specific sequence parameters.

To demonstrate the linearity of the B_1^+ estimated by SA2RAGE with the effective B_1^+ applied, the reference voltage was varied from 10 to 190 V in 19 steps. This experiment was conducted with the agar gel head phantom (dimensions: 15 cm left-right; 18 cm anterior–posterior; 21 cm top–bottom) whose geometric and electric properties created inhomogeneities significantly bigger than those found in the human head. The average estimated B_1^+ in two different regions of interest was measured in order to have enough points in the low and high transmit field regime, respectively. For comparison, the B_1^+ field was also mapped using the DAM with an echo planar imaging (EPI) (TR/TE = 30 s/15 ms, two averages, resolution = 64 × 64 × 16). The nominal flip angles α_1 and α_2 used for the DAM method were 60° and 120°, respectively, and the same variation of the reference voltage was performed. To ensure that the same region was selected for both the DAM and SA2RAGE methods, one EPI-60-degree image was coregistered to an SA2RAGE$_2$ image using FSL (26). The obtained transition matrix was subsequently applied to all the B_1^+ maps calculated with the DAM method.

To be able to estimate the interference between B_1^+ maps of different coils, it is fundamental to know both magnitude and phase of B_1^+. The phase of transmit field was assumed to be simply equal to that of the second SA2RAGE image, although it also includes B_0 field inhomogenities and reception B_1^- phase contributions, as these are the same for all the measured maps their contribution to the interference can be neglected. B_1^+ (r) was therefore assumed to be equal to $| B_1^+ (r)| e^{i \cdot \varphi(r)}$, where φ
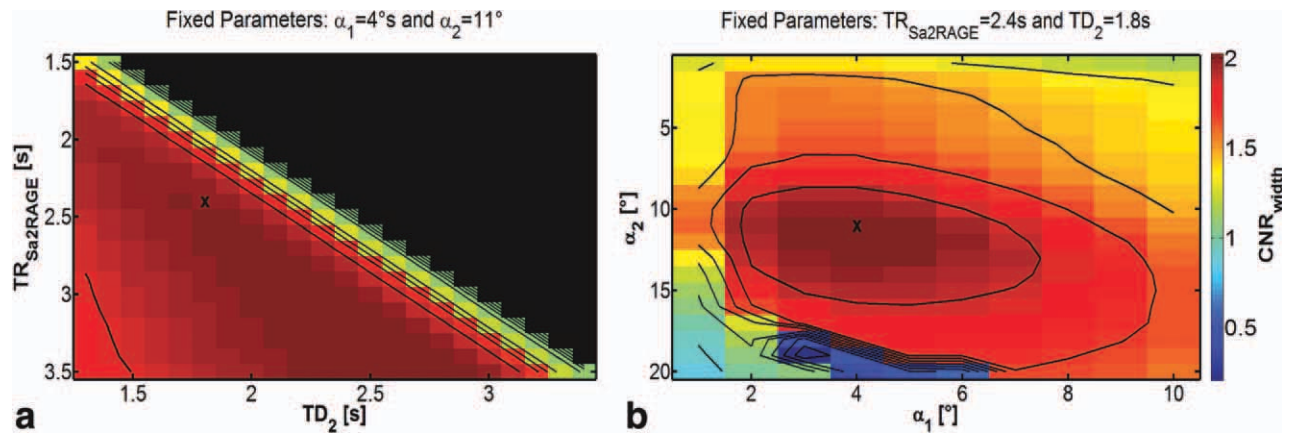
FIG. 3. Maps of CNR_{width}, defined as the width of the CNR curve above $CNR_{threshold}$, as a function of $TR_{SA2RAGE}$ and TD_2 (**a**); α_1 and α_2 (**b**). The contour lines represent isolines of CNR_{width} at 10% intervals of the maximum CNR_{width} achieved. The parameters considered optimal for the SA2RAGE sequence are represented by crosses. The black area in (a) corresponds to the forbidden region of the parameter space (TD_2 must be smaller than $TR_{SA2RAGE} - n_{aft} \cdot TR_{flash}$ ($n_{aft} = 32$)). [Color figure can be viewed in the online issue, which is available at wileyonlinelibrary.com.]

is the phase of $SA2RAGE_2$ and $|B_1^+|$ is calculated from the lookup table. To demonstrate the phase sensitivity of the SA2RAGE sequence, eight different modes were excited (transmission on all but one coil, using the same amplitude and phases as for the CP mode). Individual coil B_1^+ maps were then computed by matrix inversion (18) and compared with B_1^+ maps acquired with single coil excitations (transmission on only one coil at a time).

RESULTS

The maps presented in Figure 3 show the variation of CNR_{width}, as a function of two flip angles, TR and TD_2. CNR_{width} was defined as the width of the CNR curve above $CNR_{threshold}$ (cf. Fig. 2b). The parameters that maximize CNR_{width} were $TD_2 = 2.6$ s and $TR_{SA2RAGE} = 3.5$ s. Given that CNR_{width} is a slowly varying function, and that for the sought applications the speed of the methodology is a priority the parameters $TD_2 = 1.8$ s and $TR_{SA2RAGE} = 2.4$ s were chosen and will be used afterward, because it provides a substantial improvement in terms of acquisition time at a low cost of the CNR_{width} value.

The contrast-to-noise optimization thus led to the following optimal parameters for the SA2RAGE sequence: $TR_{SA2RAGE}/TD_1/TD_2 = 2.4$ s/0.101 s/1.8 s; $\alpha_1/\alpha_2 = 4°/11°$. This protocol (defined as—protocol A—for future references) provided a large range of precision for the B_1^+ estimations (from 0.25 to 2.25 times the nominal flip angle, see Fig. 2b). As TD_1 cannot be decreased indefinitely due to duration of the gradient echo train, the $SA2RAGE_{ratio}$ depends not only on B_1^+ but also on the different T_1s. Although this deviation is hardly noticeable in Fig. 2a for the different brain tissues, it can potentially cause a systematic error on the B_1^+ values measured, see Figure 4a.

The importance of using TD_1 as short as possible is illustrated in Figure 4b where significantly higher deviation curves are observed when $TD_1 = 200$ ms is considered. The use of 6/8 partial Fourier encoding in the phase direction implies that the center of k-space was

acquired after 16 steps instead of 32 ($n_{PE1} = 64$) allowing a decrease of TD_1 to 56 ms (protocol B). A supplementary reduction of TD_1 was achieved with the additional use of GRAPPA (acceleration factor = 2) in the same encoding direction making the minimum available TD_1 = 39 ms (Protocol C). The impact of such changes on the sensitivity to T_1 variations is illustrated in Figure 4c and d, respectively. When using protocol C, the errors introduced in WM/GM/CSF B_1^+ were estimated to be smaller than 1.6% (Fig. 4d) for a wide range of B_1^+ values (from 0.06 to 1.96) when compared with the 2.8% in the case of protocol A (Fig. 4a). It should be noted from Figure 4c and d that B_1^+-mapping is made possible even for body regions containing tissues with short T_1 values such as fat (important in the case of abdominal applications) when using either Protocol B or C. This observation reinforces the relevance of using short TD_1 values to achieve T_1 insensitivity.

Figure 5a shows the linearity of the measured B_1^+ values with the amplitude of RF voltage in the region of interest of high B_1^+ intensity compared with the rest of the phantom. The estimates obtained using the SA2RAGE sequence and the DAM are in good agreement over a large range. Divergence from linearity and a significant increase in the observed standard deviation of the measured values is noticeable at B_1^+ greater than 1.7, with the larger errors being observed for the DAM method. This increased deviation from linearity in the DAM data can be attributed to slice profile issues associated with the two-dimensional nature of the DAM method that become more noticeable as the "double angle" pulse approaches 180° and the sum of the signal excited over the slice deviates from $\sin(\alpha)$. On the other end of the B_1^+ intensity spectrum, as shown in Figure 5b (where B_1^+ values were measured in a region of lower B_1^+ intensity), it is possible to observe the increased noise at low B_1^+ values as anticipated by the left side of the CNR curve (Fig. 2b). It should also be noted that in this regime, the SA2RAGE sequence outperformed the DAM both in terms of linearity and noise behavior. It is also noteworthy that the DAM, despite the usage of an EPI readout, took 2.5 times
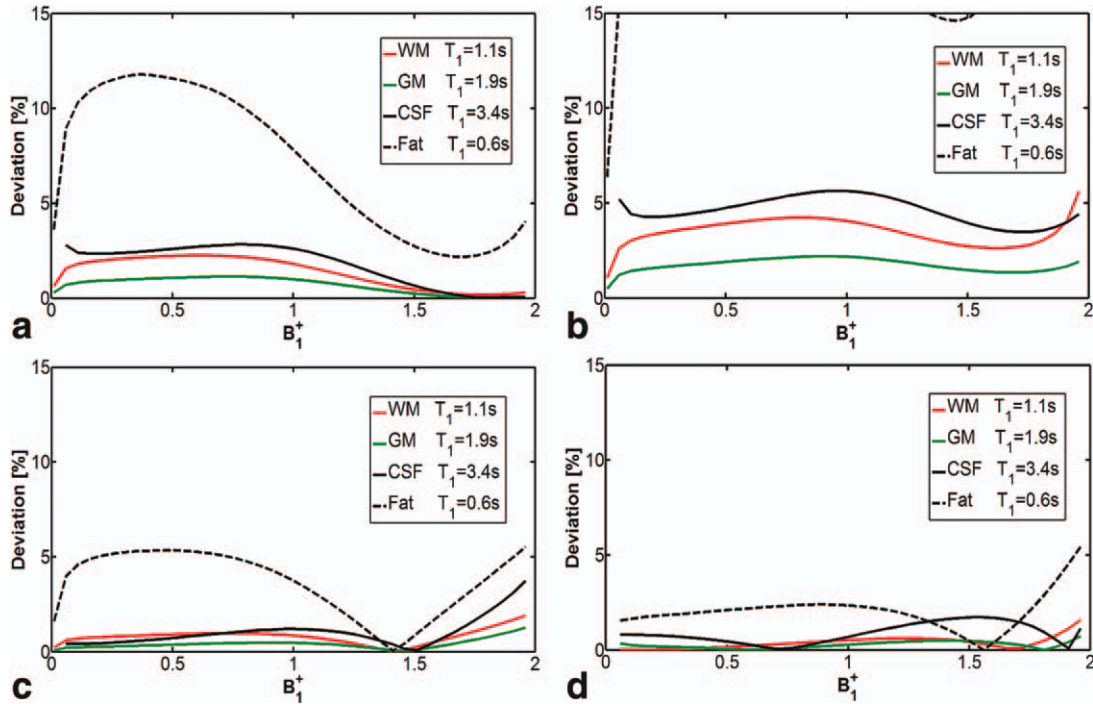
FIG. 4. Plots representing the error introduced on the estimated B_1^+ maps as a function of the B_1^+ intensity for CSF, GM, WM and fat at 7T by considering an average $T_1 = 1.5$ s. The sequence parameters for all the simulations are ($TR_{SA2RAGE}/TD_2 = 2.4/1.8$ s, $\alpha_1/\alpha_2 = 4°/11°$) while TD_1 was varied in the four plots by considering the following acquisitions: (**a**) Full k-space acquisition (Protocol A: $TD_1 = 101$ ms); (**b**) Full k-space acquisition with $TD_1 = 200$ ms; (**c**) 6/8 partial Fourier (Protocol B: $TD_1 = 56$ ms); (**d**) 6/8 partial Fourier + GRAPPA (Protocol C: $TD_1 = 39$ ms). [Color figure can be viewed in the online issue, which is available at wileyonlinelibrary.com.]

longer than the SA2RAGE acquisition. Figure 5c and d illustrates the agreement between the two mapping methods when measuring B_1^+ values up to 1.5.

Figure 6 presents the two images provided by the SA2RAGE sequence when three different protocols are used (a–f). The expected spatial pattern with a central bright spot can be observed on the corresponding brain B_1^+ maps (g–l). The increased insensitivity to T_1 variations from protocol A to C was evident on such in vivo B_1^+ maps; in Figure 6g, it is possible to visualize residual contrast between different brain tissues, such as gray and

white matter in the anterior part of the brain, whereas it is virtually vanished in Figure 6i.

Figure 7 displays B_1^+ maps with the transmit magnetic field produced by the different coils of the 8-channel transmit-receive array acquired using the parallel transmission system; it shows the good spatial agreement between the two methodologies used (top: measurement of the B_1^+ maps of the individual coils; middle row: B_1^+ maps of the individual coils calculated using the interferometry technique). This result demonstrates the phase sensitivity of the sequence, because the system of
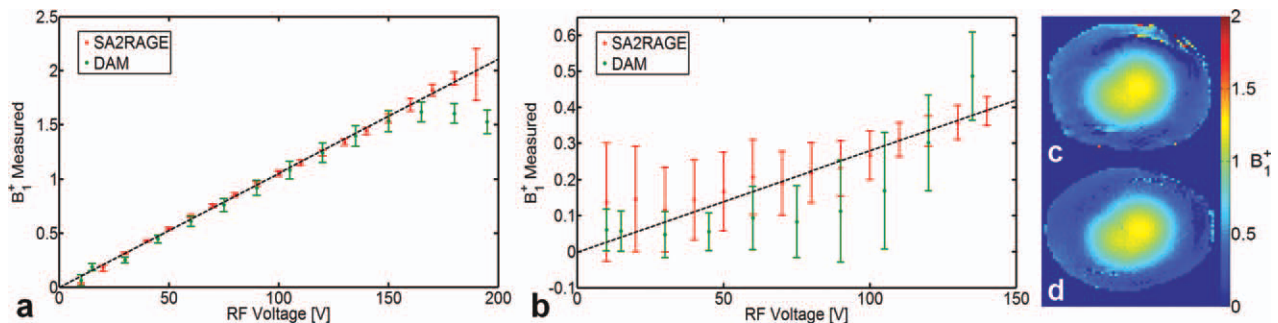

FIG. 5. Mean values and standard deviations of B_1^+ calculated using the SA2RAGE and the DAM on a ROI ($5 \times 5 \times 4$ pixels) located on different areas of an agar gel phantom as a function of the transmit reference RF voltage: (**a**) region with a relatively high B_1^+ intensity in respect to the remaining phantom - bright spot (**b**) region with low B_1^+ intensity in respect to the remaining phantom. For comparison purposes, an axial view of the B_1^+ maps obtained with (**c**) the DAM and (**d**) the SA2RAGE sequence at 120 V are shown. The scan times were 1 min 30 s and 38 s for the DAM (two measurements alternating the readout polarity were acquired to remove ghosting artifacts (34)) and the SA2RAGE sequence respectively. [Color figure can be viewed in the online issue, which is available at wileyonlinelibrary.com.]
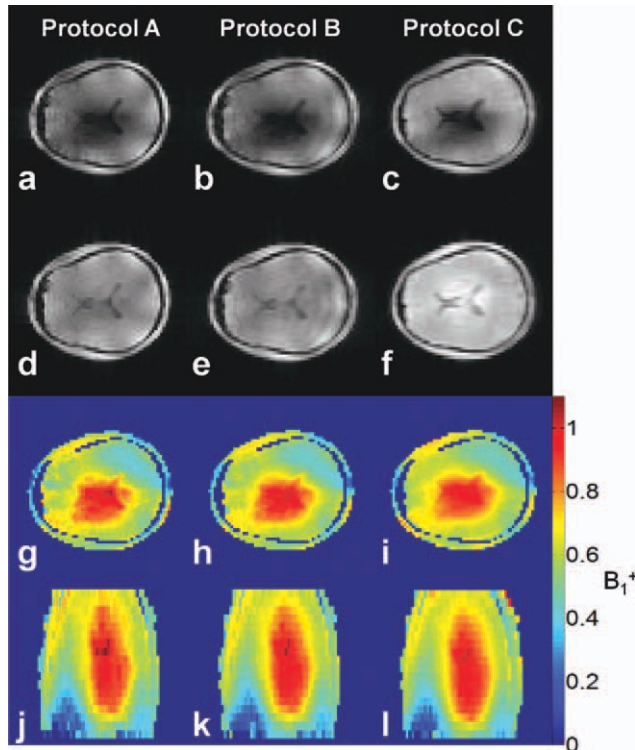
FIG. 6. Axial views of the two 3D $64 \times 64 \times 20$ images ($4 \times 4 \times 5$ mm^3 resolution) provided by the SA2RAGE sequence in 48 s with the following parameters $TR_{SA2RAGE}/TD_2 = 2.4/1.8$ s, $\alpha_1/\alpha_2 = 4°/11°$. The different columns represent the following different protocols used: first column: Full k-space acquisition (Protocol A: $TD_1 = 101$ ms); second column: 6/8 partial Fourier (Protocol B: $TD_1 = 56$ ms); third column: 6/8 partial Fourier + GRAPPA (Protocol C: $TD_1 = 39$ ms). The first (a–c) and second (d–f) rows present SA2RAGE$_1$ and SA2RAGE$_2$ images respectively, while the third (g–i) and fourth (j–l) rows present the corresponding B_1^+ maps in the transverse and coronal planes respectively. [Color figure can be viewed in the online issue, which is available at wileyonlinelibrary.com.]

equations describing the interference between the different array elements can be resolved properly only with the knowledge of the phases of the B_1^+ maps before matrix inversion. Moreover, the interferometry approach to map individual coils clearly results in a lower noise

level present in the coil profiles acquired with the SA2R-AGE method. Bottom row in Figure 7 shows the B_1^+ maps of the individual coils calculated using the interferometry method on a volunteer with the total acquisition time of ~5 min without exceeding the SAR constraints mentioned in the methods section.

DISCUSSION

A new sequence to map the transmit magnetic field in a 3D manner was introduced in this work. Its short acquisition time and low SAR characteristics as well as its wide range of accuracy make it a valuable tool to quantitatively map the transmit field B_1^+ in vivo at high fields. It should be highlighted that the short acquisition times needed to obtain the B_1^+ maps in this work did not rely on EPI readout. Such readout, as used to accelerate the DAM, poses serious limitations in vivo because of its high sensitivity to physiological noise (due to the inherently longer TE), which will affect the precision of the calculated transmit field.

The limiting factor in terms of acquisition time of the current B_1^+ map calculation is the number of repetitions performed and used to encode the different slices. The lookup table created to estimate the B_1^+ field relies on the assumption that steady state is achieved (see Appendix 1); it is interesting to note that the B_1^+ estimation converges to that of the steady state extremely quickly. This observation was made via simulations considering the process of driving the magnetization from fully relaxed through various repetitions of the SA2RAGE sequence towards steady state. During the second repetition, the estimated B_1^+ field had a maximum deviation from the steady state estimation of 3% (at the third repetition, the maximum deviation was already under 0.4%). This observation implies that the SA2RAGE method could be used for 3D acquisitions with as few as 4 to 8 repetitions, which would bring the total time to acquire a 3D B_1^+ map down to 9.5 or 19 s, respectively. Another important assumption of the lookup table is that the signal of each image is fully described by the intensity of the echo corresponding to the central k-space plane. As the local B_1^+ increases, the higher the flip angles are and
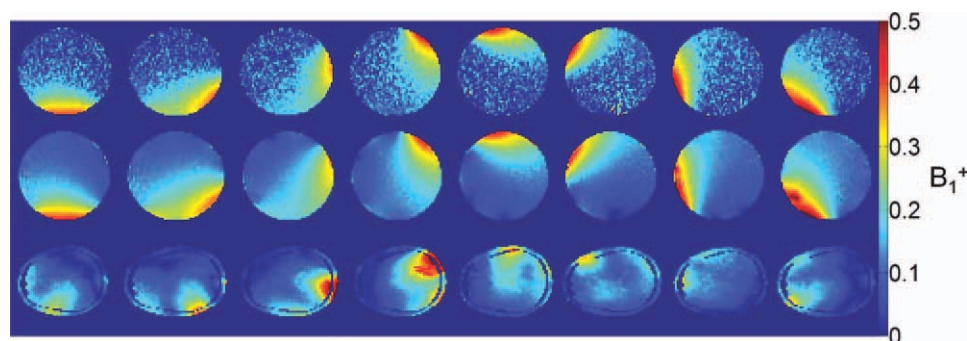

FIG. 7. Axial views ($z = 8$) of $64 \times 64 \times 16$ pixel images corresponding to the B_1^+ profiles produced by each individual coil on an oil phantom (top and middle row) and on a human head (bottom row). On the top row only one activated coil was measured at a time. On the middle and bottom rows, the B_1^+ map of each array element was measured by means of interferometry using all but one coil active. The scan time for each image was 38 s ($TR_{SA2RAGE} = 2.4$ s). [Color figure can be viewed in the online issue, which is available at wileyonlinelibrary.com.]

hence the intensity between the different *k*-space lines will change more rapidly, increasing the point spread function weighing in the phase encoding direction. This effect could be responsible for the deviation from the linear relation in the SA2RAGE sequence visible for high B_1^+ values (see Fig. 5a). However, it should be noted that the deviation for high nominal B_1^+ values was smaller than the one observed with the DAM method. Reducing the number of excitations and the duration of the GRE block will mitigate possible consequences to the point spread function stemming from both saturation and T_1 relaxation. One last assumption of the SA2RAGE sequence is that the signal is ideally spoiled throughout the GRE readout periods. Deviations from ideal spoiling are expected to be observable at high B_1^+ values, with the effective flip angle of the second GRE block being as high as 22° (for a $B_1^+ = 2$). The validity of this assumption is extensively evaluated and confirmed through simulations, calibration studies, and in vivo data acquisitions in Appendix 2.

As discussed in the introduction, many B_1^+-mapping techniques are sensitive to the varying T_1 values found in different tissues and this dependence can be mitigated by either using long repetition times or designing the mapping method in such a way that both B_1^+ and T_1 values are measured. As shown in Figure 4a, c, and d, for the typical T_1 values found in the human brain, the optimal parameters make the estimate of the transmit field virtually insensitive to variations in the longitudinal relaxation times (<3 and <1.7%, respectively). With the insensitivity to T_1 achieved by using parallel imaging (Fig. 4d), it is possible to state that this B_1^+-mapping scheme could find applications also in the domain of abdominal imaging. Moreover, it is possible to further reduce the sensitivity to T_1 by decreasing the TD$_1$ time. Such a reduction could be achieved in several ways: either by reducing the number of phase encoding steps (by further parallel imaging acceleration or decreasing the resolution), or by increasing the number of phase-encoded lines per excitation (and hence reducing the number of time consuming slab-selective excitation pulses). In case the whole sensitive volume of the coil is to be acquired, the slab-selective pulses can be replaced by shorter hard pulses, which will also contribute to the reduction of TD$_1$. One other approach to reduce the T_1 sensitivity of the SA2RAGE sequence, by reducing TD$_1$, would be to use a centric phase encoding. Such an approach was not pursued due to the significantly increased blurring on the phase encoding direction when compared with that introduced by linear phase encoding (27,28). While the blurring might be rather benign at the center of the image (as the B_1^+ map is not expected to present fast spatial variations), at the edges, this effect would be more pronounced. Furthermore, the amount of blurring would be B_1^+ dependent, increasing with increasing B_1^+ values which accentuate the PSF via the increased signal saturation $\cos^n(\alpha B_1^+)$ and via the faster longitudinal recovery $(1 - 2\cos(\pi/2.B_1^+)\exp(-TD/T_1))$.

CONCLUSIONS

The SA2RAGE sequence can be used to accurately and quantitatively map the B_1^+ field within a 3D volume in less than 30 s. The wide range of validity experimentally observed from $B_1^+ = 0.2 - 2.0$ should also be noted. The accuracy of the SA2RAGE and insensitivity to the range of T_1 values observed in the brain (<3%) is acceptable for most B_1^+-mapping applications and was shown to be further improvable by using partial Fourier sampling schemes. SA2RAGE is thus a promising tool for fast and accurate B_1^+-mapping, of particular interest for applications using multichannel transmission. In our current implementation it is possible to obtain B_1^+ maps online, making it an important tool during the scan setup process.

APPENDIX A

The SA2RAGE sequence is characterized simply by three types of periods that affect the longitudinal magnetization in the following way:

(a) Longitudinal magnetization is saturated by means of an hard pulse, meaning that

$$M_{z,\text{sat}}\left(M_z(0), B_1^+\right) = M_z(0)\cos\left(\frac{\pi}{2}B_1^+\right) \quad [A1]$$

(b) During the GRE blocks of *n* RF pulses with constant flip angles α, separated by an interval TR, the longitudinal magnetization evolves in the following way (29):

$$M_{z,n\text{RF}}\left(M_z(0), T_1, n, TR, \alpha B_1^+\right)$$
$$= M_z(0)\left(\cos(\alpha B_1^+)e^{-TR/T_1}\right)^n$$
$$+ M_o(1 - e^{TR/T_1})\frac{1 - \left(\cos(\alpha B_1^+)e^{-TR/T_1}\right)^n}{1 - \cos(\alpha B_1^+)e^{-TR/T_1}} \quad [A2]$$

where $M_z(0)$ is the longitudinal magnetization at the start of the RF free periods.

(c) During the periods with no RF pulses, the longitudinal magnetization relaxes freely towards equilibrium following the conventional T_1 relaxation expression:

$$M_{z,0RF}(M_z(0), T_1, t) = M_z(0)e^{-t/T_1} + M_o(1 - e^{-t/T_1}) \quad [A3]$$

A full account of the signal resulting from the SA2RAGE sequence has to take into account the steady state condition. This implies that the longitudinal magnetization before successive saturations, $m_{z,ss}$, has to be the same. Between two successive saturations, the $m_{z,ss}$, undergoes first one saturation (a), followed by recovery for a period TA (c), a first GRE block (b), a free recovery for a period TB (c), a second GRE block (b), and a final recovery for a period TC (c) by the end of which it should be back to its initial value. Mathematically, it is equivalent to solve the following composite equation:

$$m_{z,ss} = M_{z,0rf}(M_{z,nrf}(M_{z,0rf}(M_{z,nrf}(M_{z,0rf}(M_{z,sat}(m_{z,ss}, B_1^+), T_1, TA), T_1, n, TR, \alpha_1 B_1^+), T_1, TB), T_1, n, TR, \alpha_2 B_1^+), T_1, TC) \quad \text{[A4]}$$

where TA, TB, and TC are the delays in between the saturation and the start of the first GRE block, between the two GRE blocks and from the end of the second GRE block to the saturation pulse, respectively. Solving this equation for $m_{z,ss}$ results in the following steady state:

$$m_{z,ss} = M_0 \frac{\left[\left(\left((1-EA)(\cos(\alpha_1 B_1^+)E1)^n + (1-E1)\frac{1-(\cos(\alpha_1 B_1^+)E1)^n}{1-\cos(\alpha_1 B_1^+)E1} \right) EB + (1-EB) \right) (\cos(\alpha_2)E1)^n + (1-E1)\frac{1-(\cos(\alpha_2 B_1^+)E1)^n}{1-\cos(\alpha_2 B_1^+)E1} \right] EC + (1-EC)}{1 - \cos\left(\frac{\pi}{2}B_1^+\right)(\cos(\alpha_1 B_1^+)\cos(\alpha_2 B_1^+))^n e^{-TR_{Sa2RAGE}/T_1}}$$

[A5]

where $E_1 = \exp(-TR/T_1)$, $EA = \exp(-TA/T_1)$, $EB = \exp(-TB/T_1)$, and $EC = \exp(-TC/T_1)$.

Once the steady state condition is known, the signal for each of the images can be expressed as:

$$SA2RAGE_1 = B_1^- e^{-TE/T_2^*} e^{-i\Delta\omega TE} M_o \sin(\alpha_1 B_1^+)$$
$$\times \left[\left(\frac{\cos\left(\frac{\pi}{2}B_1^+\right) \cdot m_{z,SS}}{M_o} EA + (1-EA) \right) (\cos(\alpha_1 B_1^+)E1)^{n_{bef}} + (1-E1)\frac{1 - (\cos(\alpha_1 B_1^+)E1)^{n_{bef}}}{1 - \cos(\alpha_1 B_1^+)E1} \right]$$
$$SA2RAGE_2 = B_1^- e^{-TE/T_2^*} e^{-i\Delta\omega TE} M_o \sin(\alpha_2 B_1^+) \left[\frac{\frac{m_{z,SS}}{M_o} - (1-EC)}{EC(\cos(\alpha_2 B_1^+)E1)^{n_{aft}}} - (1-E1)\frac{(\cos(\alpha_2 B_1^+)E1)^{n_{aft}} - 1}{1 - \cos(\alpha_2 B_1^+)E1} \right] \quad \text{[A6]}$$

where n_{bef} and n_{aft} stand for the number of phase encoding steps before and after the k-space center is excited (in the case of full k-space coverage $n_{bef} = n/2 - 1$ and $n_{aft} = n/2$). From Eq. A6, it is clear that when combining the two different images to generate the SA2RAGE ratio image the dependence in M_0, T_2^*, and $\Delta\omega$ will disappear, whereas only B_1^+ and T_1 dependences will remain. The lookup tables from which B_1^+ values were subsequently computed were based on the ratio between SA2RAGE$_1$ and SA2RAGE$_2$ as described in Eq. A6.

To understand the general trends of the SA2RAGE ratio to a first order, consider: the low flip angle regime (where $\sin(\alpha B_1^+) \sim \alpha B_1^+$ and $\cos(\alpha B_1^+) \sim 1$); EA = E_1 = EC = 1. The ratio between the two images will thus be simply given by $\frac{\alpha_1}{\alpha_2}\cos\left(\frac{\pi}{2}B_1^+\right)$, meaning that either positive or negative values of the ratio are observed when the relative B_1^+ amplitude is smaller or bigger than one, respectively.

APPENDIX B

Equations A1–A6 are valid only if the transverse magnetization before each excitation or saturation in the SA2RAGE sequence can be neglected. This approximation can only be done if an efficient gradient and RF spoiling scheme is applied. In order to determine the most suitable scheme, simulations considering gradient spoiling after each excitation pulse (cf. Fig. 1) as well as RF spoiling were performed for the SA2RAGE sequence as described in Ref. 24. Simulations were performed considering an average $T_1 = 1.5$ s and an average $T_2 = 100$ ms. It should be noted that this T_2, in the context of brain imaging at 7T, is rather large (T_2^* values in white

and grey matter vary from 18–33 ms (30)). Such a long T_2 was chosen so that an upper bound of the problem could be estimated. The magnetization (M_x, M_y, M_z) at the very beginning of the sequence was considered as being fully relaxed ($M_x = 0$, $M_y = 0$, $M_z = 1$). The transverse magnetization was only ignored after the saturation pulse, which is followed by a strong crusher gradient (cf. Fig. 1) different from the crushers applied after each readout gradient. Within each GRE block, the effects of the excitation pulses of flip angles α_1 (and α_2) were taken into account via a matrix formalism simulating a rotation of the magnetization (M_x, M_y, M_z) by a flip angle $B_1^+ \cdot \alpha_1$ ($B_1^+ \cdot \alpha_2$ for the second GRE block) around an axis defined by the phase ϕ of the RF spoiling scheme. This phase increases from the nth excitation pulse of the GRE block to the nth + 1 according to (31): $\phi_{n+1} - \phi_n = n\Delta\Phi$ ($n \in [1, n_{PE1}]$). T_1 and T_2 relaxations were also simulated between each excitation pulse. The spoiling gradient applied after each readout gradient was taken into account by considering a rotation of the magnetization vector around the z axis by an angle Ω. Note that Ω was varied from 4° to 360° in steps of 4° in order to simulate different isochromats. This SA2RAGE simulation was repeated for three TRs in order to reach the steady-state. At the end of the simulation, the sum over all isochromats was performed for each phase encoding step to obtain a macroscopic value for the magnetization. The simulation was repeated for $\Delta\Phi$ values ranging from 0° to 180° in steps of 0.1°, and for B_1^+ values varying from 0.01 to 2.11.

Two different methodologies were used to evaluate the optimum RF spoiling scheme. In the first methodology, the SA2RAGE$_{ratio}$ was calculated considering the k-space
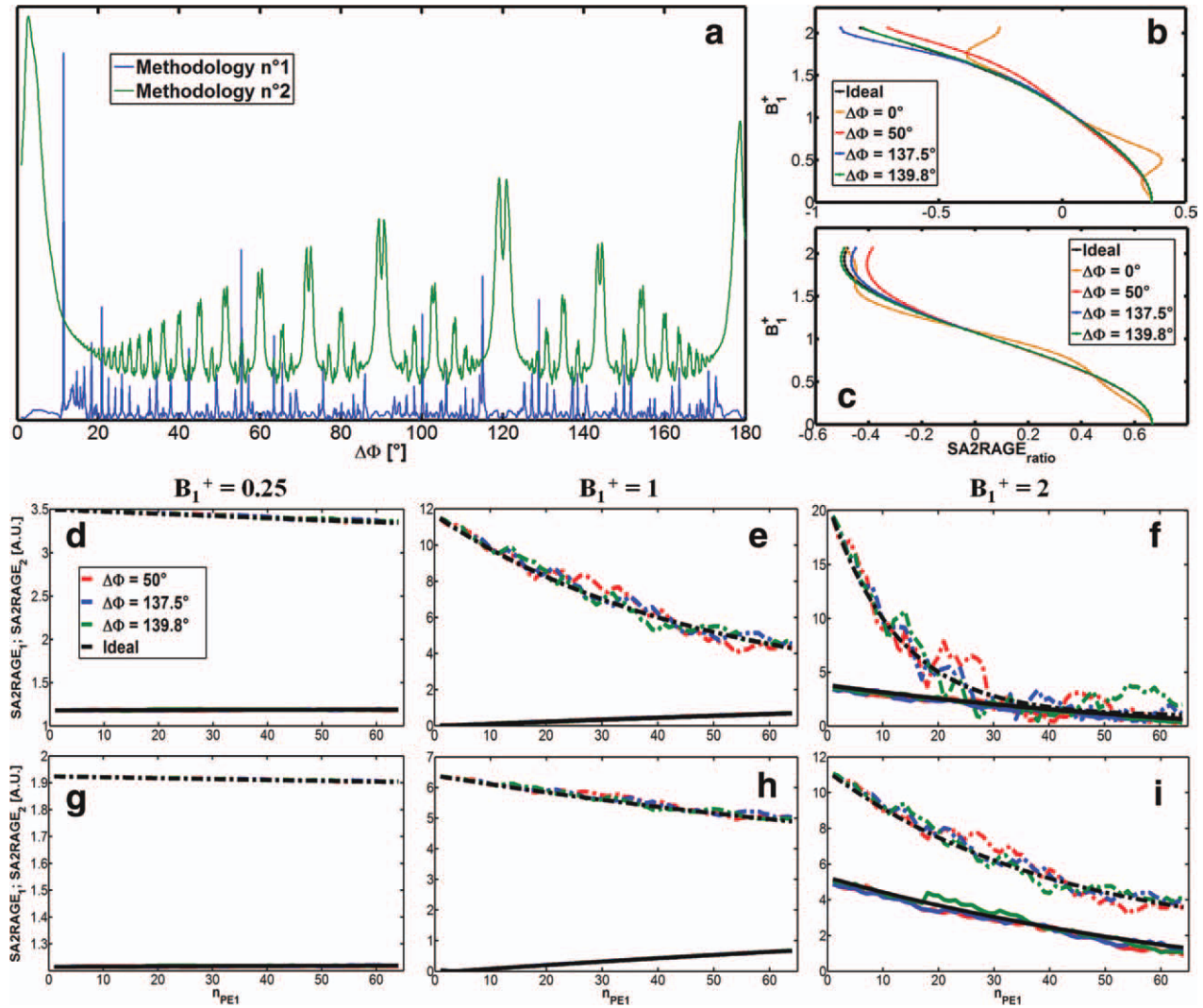
FIG. B1. **a**: Plot showing the deviation from the ideally spoiled SA2RAGE sequence (using Protocol A) as a function of the RF spoiling phase increment. Deviation was computed considering the norm of the difference between ideal and simulated SA2RAGE$_{ratio}$ (Methodology 1) and the sum of the squared difference between the ideal and simulated SA2RAGE$_2$ over all phase encoding steps and B_1^+ values (Methodology 2). SA2RAGE lookup tables simulated for different RF spoiling phase increments and ideally spoiled using: (**b**) protocol A and (**c**) a smaller flip angle protocol ($\alpha_2 = 6°$ and otherwise equivalent to protocol A). Plots showing the magnitude of the signal ofSA2RAGE$_1$ (full lines) and SA2RAGE$_2$ (dashed lines) as a function of the phase encoding steps for a B_1^+ of 0.25 (**d,g**), 1 (**e,h**), and 2 (**f,i**) for protocol A (d,e,f) and the small flip angle protocol (g,h,i). [Color figure can be viewed in the online issue, which is available at wileyonlinelibrary.com.]

centre excitation for the simulated range of B_1^+, and for each specific $\Delta\Phi$. The different lookup tables were then compared with the analytical one resulting from Eq. A1–A6. In the second methodology, the RF spoiling was evaluated by considering, for each RF spoiling phase increment, the sum over the simulated B_1 values and all the 64-phase encoding steps of the square difference between the simulated SA2RAGE$_2$ signal and the analytical expression. While the first methodology favours RF spoiling schemes that provide a good result at the *k*-space centre (although this might be dependent on the T_2 value and number of phase encoding steps), the second methodology favors a scheme with less fluctuations over all the phase encoding steps. These two metrics produce different patterns, see Figure B1(a). For the first methodology, the ideal RF spoiling scheme was found to be $\Delta\Phi = 139.8°$, while the second methodology had an

optimum RF spoiling phase increment of $137.5°$. It should be noted that the RF phase spoiling patterns obtained with the second methodology are in close agreement with those of conventional GRE sequence (see Fig. 1 of Ref. 24), the actual flip angle imaging sequence (see Fig. 2 of Ref. 32) and the steady state preparation (see Fig. 9 of Ref. 33).

Three different RF spoiling increments were evaluated both from a theoretical, an experimental calibration and human applications perspective. The three evaluated RF spoiling phase increments were: $50°$ (the standard Siemens RF spoiling phase increment, originally suggested by Preibisch et al. (24) and used throughout the article); $139.8°$ (to optimize the SA2RAGE$_{ratio}$ accuracy—Methodology 1) and $137.5°$ (to optimize the stability of SA2RAGE$_2$ over the various phase encoding steps—Methodology 2).
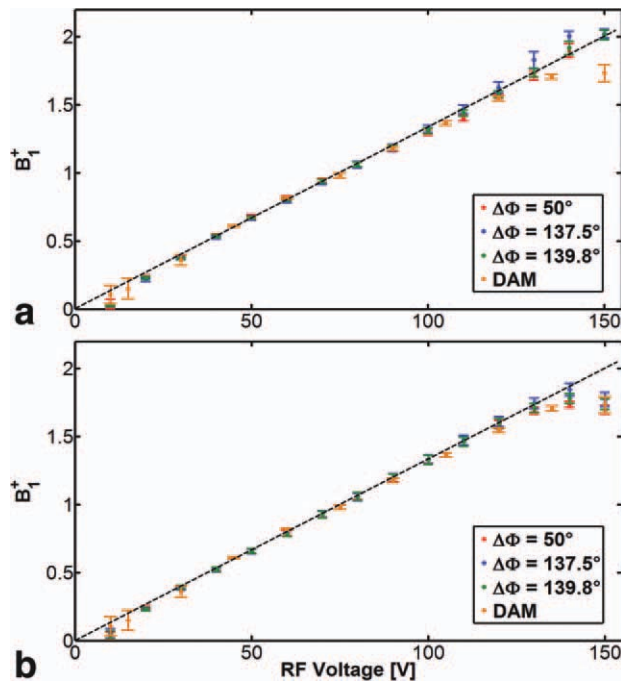
FIG. B2. Mean values and standard deviations of B_1^+ calculated using the SA2RAGE sequence on a ROI ($5 \times 5 \times 4$ pixels) of an agar gel phantom as a function of the transmit reference RF voltage using (**a**) protocol A and (**b**) the small flip angle variation of protocol A ($\alpha_2 = 6°$). The different colours correspond to different RF spoiling phase increments ($50°$, $137.5°$, and $139.8°$). [Colour figure can be viewed in the online issue which is available at wileyonlinelibrary.com.]

In terms of theoretical SA2RAGE$_{ratio}$ fidelity, Figure B1(b) shows the expected trend, with the RF spoiling phase with the best match being that obtained using Methodology 1, but with very satisfactory results being obtained using the two remaining phase increments (although very different results are observed in the absence of RF spoiling). It is also clear that, by reducing the amplitude of the flip angle used in the second readout from $11°$ to $6°$, the importance to use an appropriate

phase cycling is significantly reduced with all methods showing acceptable results. Figures B1(d–f) demonstrate that the fluctuations observed throughout the GRE train increase with the increase of the B_1^+ value (which increases the effective flip angle) and are minimized for a phase increment of $137.5°$ as expected from the simulations [see Fig. B1(a)]. Such fluctuations can be significantly reduced by selecting a protocol with smaller flip angles [see Fig. B1(g–i)]. Note that these fluctuations are calculated considering a $T_2 = 100$ ms, which is likely to represent a worst case scenario in the context of high field imaging.

Figure B2 shows calibration curves obtained in a phantom experiment (identical to that described for Fig. 5) for the protocol with the large flip angle [$\alpha_2 = 11°$, Fig. B2(a)] and for the protocol with small flip angle [$\alpha_2 = 6°$, Fig. B2(b)] using the three evaluated RF spoiling phase increments. No significant differences are observable between the various RF spoiling methodologies. Nevertheless, it should be noted that the differences observed for high reference voltages (and hence B_1^+ values) was in agreement with the behaviour predicted by the simulations [see Fig. B1(b)]. The RF spoiling schemes with $50°$ and $137.5°$ underestimate and overestimate B_1^+ values measured with the ideal spoiling and the $139.8°$ phase increment. Furthermore, using the SA2RAGE sequence with $\alpha_2 = 6°$ implies a shortening of the range over which B_1^+ can be accurately measured [more than 20% loss in CNR$_{width}$ if α_2 is reduced from $11°$ to $6°$ as can be seen in Fig. 3b and from the earlier deviation from linearity in Fig. B2(b) than in Fig. B2(a)].

Figure B3 shows in vivo B_1^+ maps obtained with different RF spoiling phase increments. The differences between the tested RF spoiling increments are minor [see Figs. B3(b–d)], while using no RF spoiling introduced significant errors on the estimated B_1^+ values [see Fig. B3(a)]. Again, the need to use RF spoiling decreases significantly as α_2 is made smaller (the bottom rows of Figures B2 and B3 were obtained with $\alpha_2 = 6°$, implying that for a relative $B_1^+ = 2$, the effective $\alpha_2 = 12°$). Note that the in vivo B_1^+ map obtained in the absence of RF
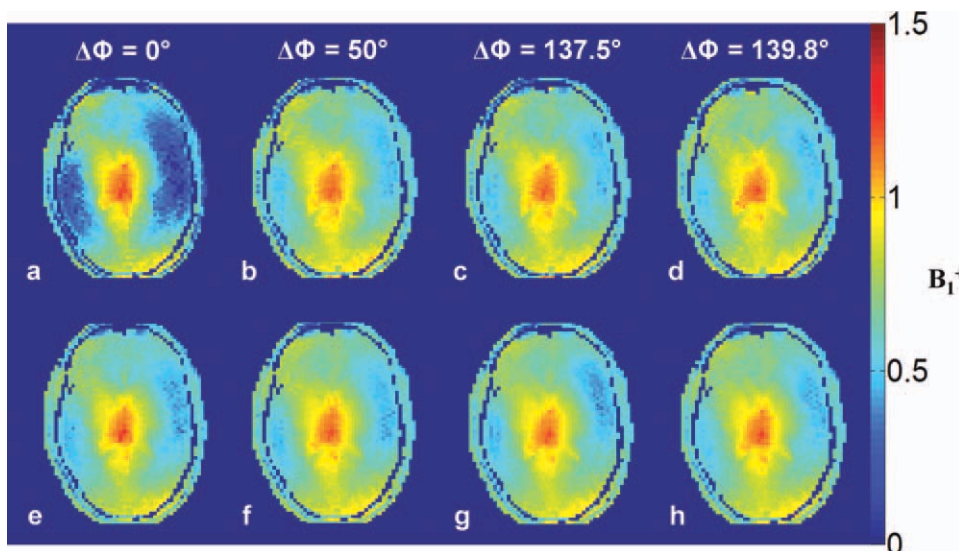

FIG. B3. Axial views of 3D in vivo B_1^+ maps ($4 \times 4 \times 5$ mm^3 resolution, $64 \times 64 \times 20$ matrix) calculated by the SA2RAGE sequence in 48 s with the following parameters: TR$_{SA2RAGE}$/TD$_2$=2.4/1.8s, α_1/α_2=4°/11° (top) and α_1/α_2=4°/6° (bottom). Each column is related to a specific RF spoiling phase increment $\Delta\Phi$: $\Delta\Phi$=0° (**a,e**); $\Delta\Phi$=50° (**b,f**); $\Delta\Phi$=137.5° (**c,g**); $\Delta\Phi$=139.8° (**d,h**). [Colour figure can be viewed in the online issue which is available at wileyonlinelibrary.com.]

spoiling with small flip angles [Fig. B3(e)] closely resembles the B_1^+ maps obtained using the optimized RF spoiling schemes.

This appendix demonstrates both the importance of using an appropriate RF spoiling to obtain accurate B_1^+ values, but also that a large number of possible choices exist that have a small impact on the outcome of the measured B_1^+. It should be noted that the three spoiling options evaluated are close to optimal in both evaluated metrics.

REFERENCES

1. Hoult DI, Phil D. Sensitivity and power deposition in a high-field imaging experiment. J Magn Reson Imaging 2000;12:46–67.
2. Katscher U, Bornert P, Leussler C, van den Brink JS. Transmit SENSE. Magn Reson Med 2003;49:144–150.
3. Zhu Y. Parallel excitation with an array of transmit coils. Magn Reson Med 2004;51:775–784.
4. Setsompop K, Alagappan V, Gagoski B, Witzel T, Polimeni J, Potthast A, Hebrank F, Fontius U, Schmitt F, Wald LL, Adalsteinsson E. Slice-selective RF pulses for in vivo B_1^+ inhomogeneity mitigation at 7 tesla using parallel RF excitation with a 16-element coil. Magn Reson Med 2008;60:1422–1432.
5. Stollberger R, Wach P. Imaging of the active B$_1$ field in vivo. Magn Reson Med 1996;35:246–251.
6. Akoka S, Franconi F, Seguin F, Le Pape A. Radiofrequency map of an NMR coil by imaging. Mag Reson Imaging 1993;11:437–441.
7. Jiru F, Klose U. Fast 3D radiofrequency field mapping using echoplanar imaging. Magn Reson Med 2006;56:1375–1379.
8. Yarnykh VL. Actual flip-angle imaging in the pulsed steady state: a method for rapid three-dimensional mapping of the transmitted radiofrequency field. Magn Reson Med 2007;57:192–200.
9. Dowell NG, Tofts PS. Fast, accurate, and precise mapping of the RF field in vivo using the 180 degrees signal null. Magn Reson Med 2007;58:622–630.
10. Oh CH, Hilal SK, Cho ZH, Mun IK. Radio frequency field intensity mapping using a composite spin-echo sequence. Magn Reson Imaging 1990;8:21–25.
11. Morrell GR. A phase-sensitive method of flip angle mapping. Magn Reson Med 2008;60:889–894.
12. Fleysher R, Fleysher L, Liu S, Gonen O. TriTone: a radiofrequency field (B$_1$)-insensitive T$_1$ estimator for MRI at high magnetic fields. Magn Reson Imaging 2008;26:781–789.
13. Hsu JJ, Zaharchuk G, Glover GH. Rapid methods for concurrent measurement of the RF-pulse flip angle and the longitudinal relaxation time. Magn Reson Med 2009;61:1319–1325.
14. Wang J, Qiu M, Yang QX, Smith MB, Constable RT. Measurement and correction of transmitter and receiver induced nonuniformities in vivo. Magn Reson Med 2005;53:408–417.
15. Wang J, Mao W, Qiu M, Smith MB, Constable RT. Factors influencing flip angle mapping in MRI: RF pulse shape, slice-select gradients, off-resonance excitation, and B$_0$ inhomogeneities. Magn Reson Med 2006;56:463–468.
16. Setsompop K, Wald LL, Alagappan V, Gagoski B, Hebrank F, Fontius U, Schmitt F, Adalsteinsson E. Parallel RF transmission with eight channels at 3 Tesla. Magn Reson Med 2006;56:1163–1171.
17. Chung S, Kim D, Breton E, Axel L. Rapid B_1^+ mapping using a preconditioning RF pulse with TurboFLASH readout. Magn Reson Med 2010;64:439–446.
18. Brunner DO, Pruessmann KP. B_1^+ interferometry for the calibration of RF transmitter arrays. Magn Reson Med 2009;61:1480–1488.
19. Marques JP, Kober T, Krueger G, van der Zwaag W, Van de Moortele PF, Gruetter R. MP2RAGE, a self bias-field corrected sequence for improved segmentation and T$_1$-mapping at high field. Neuroimage 2010;49:1271–1281.
20. Vaughan JT, Garwood M, Collins CM, Liu W, DelaBarre L, Adriany G, Andersen P, Merkle H, Goebel R, Smith MB, Ugurbil K. 7T vs. 4T: RF power, homogeneity, and signal-to-noise comparison in head images. Magn Reson Med 2001;46:24–30.
21. Malik SJ, Larkman DJ, Hajnal JV. Optimal linear combinations of array elements for B$_1$ mapping. Magn Reson Med 2009;62:902–909.
22. Deichmann R. Fast high-resolution T$_1$ mapping of the human brain. Magn Reson Med 2005;54:20–27.
23. Cunningham CH, Pauly JM, Nayak KS. Saturated double-angle method for rapid B_1^+ mapping. Magn Reson Med 2006;55:1326–1333.
24. Preibisch C, Deichmann R. Influence of RF spoiling on the stability and accuracy of T1 mapping based on spoiled FLASH with varying flip angles. Magn Reson Med 2009;61:125–135.
25. Griswold MA, Jakob PM, Heidemann RM, Nittka M, Jellus V, Wang J, Kiefer B, Haase A. Generalized autocalibrating partially parallel acquisitions (GRAPPA). Magn Reson Med 2002;47:1202–1210.
26. Jenkinson M, Bannister P, Brady M, Smith S. Improved optimization for the robust and accurate linear registration and motion correction of brain images. Neuroimage 2002;17:825–841.
27. Deichmann R, Good CD, Josephs O, Ashburner J, Turner R. Optimization of 3-D MP-RAGE sequences for structural brain imaging. Neuroimage 2000;12:112–127.
28. Stocker T, Shah NJ. MP-SAGE: a new MP-RAGE sequence with enhanced SNR and CNR for brain imaging utilizing square-spiral phase encoding and variable flip angles. Magn Reson Med 2006;56:824–834.
29. Deichmann R, Haase A. Quantification of T1 values by snapshot-flash NMR imaging. J Magn Reson 1992;96:608–612.
30. Peters AM, Brookes MJ, Hoogenraad FG, Gowland PA, Francis ST, Morris PG, Bowtell R. T2* measurements in human brain at 1.5, 3 and 7 T. Magn Reson Imaging 2007;25:748–753.
31. Zur Y, Wood ML, Neuringer LJ. Spoiling of transverse magnetization in steady-state sequences. Magn Reson Med 1991;21:251–263.
32. Yarnykh VL. Optimal radiofrequency and gradient spoiling for improved accuracy of T1 and B_1 measurements using fast steady-state techniques. Magn Reson Med 2010;63:1610–1626.
33. Busse RF, Riederer SJ. Steady-state preparation for spoiled gradient echo imaging. Magn Reson Med 2001;45:653–661.
34. van der Zwaag W, Marques JP, Lei H, Just N, Kober T, Gruetter R. Minimization of Nyquist ghosting for echo-planar imaging at ultra-high fields based on a "negative readout gradient" strategy. J Magn Reson Imaging 2009;30:1171–1178.